The role of dyking and fault control in the rapid onset of eruption at Chaitén volcano, Chile

Charles Wicks[1], Juan Carlos de la Llera[2], Luis E. Lara[3] & Jacob Lowenstern[1]

[1]US Geological Survey, Menlo Park, CA 94025, USA. [2]Escuela de Ingeniería, Pontificia Universidad Católica de Chile, Santiago 7820436, Chile. [3]Servicio Nacional de Geología y Minería, Volcano Hazards Program, Santiago 8320119., Chile.

Rhyolite is the most viscous of liquid magmas, so it was surprising that on 2 May 2008 at Chaitén Volcano, located in Chile's southern Andean volcanic zone, rhyolitic magma migrated from more than 5 km depth in less than 4 hours (ref. 1) and erupted explosively with only two days of detected precursory seismic activity[2]. The last major rhyolite eruption before that at Chaitén was the largest volcanic eruption in the twentieth century, at Novarupta volcano, Alaska, in 1912. Because of the historically rare and explosive nature of rhyolite eruptions and because of the surprisingly short warning before the eruption of the Chaitén volcano, any information about the workings of the magmatic system at Chaitén, and rhyolitic systems in general, is important from both the scientific and hazard perspectives. Here we present surface deformation data related to the Chaitén eruption based on radar interferometry observations from the Japan Aerospace Exploration Agency (JAXA) DAICHI (ALOS) satellite. The data on this explosive rhyolite eruption indicate that the rapid ascent of rhyolite occurred through dyking and that melt segregation and magma storage were controlled by existing faults.

Chaitén volcano is situated on a forearc sliver between the Chile–Peru subduction zone and the Liquiñe–Ofqui fault zone (LOFZ; Fig. 1). The LOFZ is a long-lived shear zone[3] that has accommodated transpressional (northward translational and eastward compressional) movement of the forearc sliver for at least the past ~4 Myr (refs 4, 5). Chaitén has a caldera roughly 3 km in diameter that is part of the Michimahuida–Chaitén volcanic complex (Fig. 1). The dacitic to basaltic Michimahuida volcano, located in the LOFZ about 15 km east of Chaitén, has a larger caldera about 8 km in diameter that probably formed in the Early Holocene and was subsequently filled by dacite and later basalt effusions[6].

Although the study area is heavily vegetated and the time intervals between acquisitions are long, the 23.6-cm wavelength of the radar instrument enabled us to calculate useful interferograms (Fig. 1b–d and Supplementary Figs 1 and 2). In 2010 JAXA acquired descending-mode radar data, enabling the calculation of descending-mode interferograms; the most coherent one is shown in Fig. 1d. Together the two ascending-mode interferograms in Fig. 1b, c span the time interval covered by the descending-mode interferogram shown in Fig. 1d. The descending-mode interferogram displays a broad area of movement (about 50 cm maximum) away from the satellite that encompasses the entire Michimahuida–Chaitén volcanic complex; it is not visible in

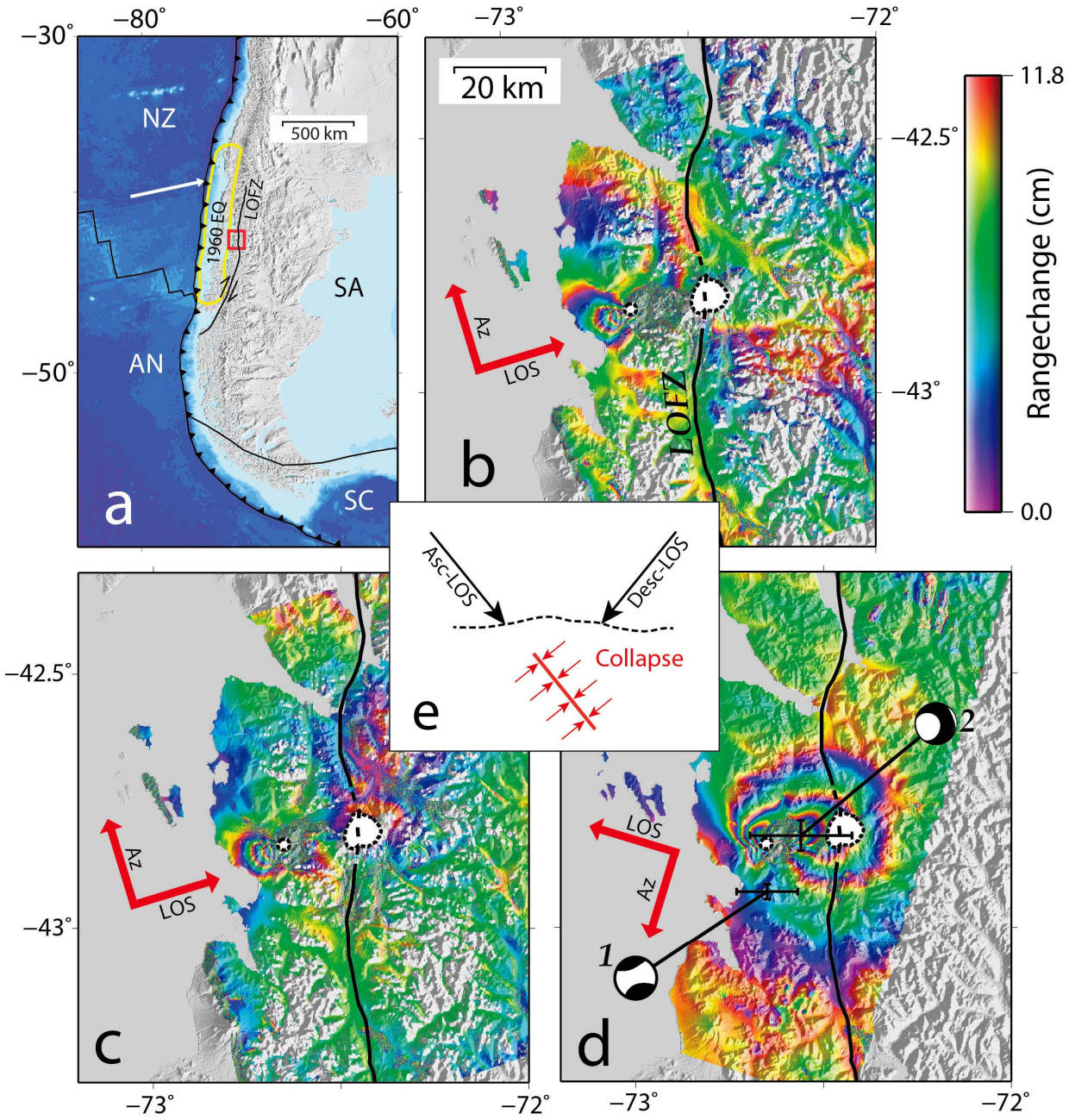

Figure 1 | Tectonic setting for Chaitén Volcano and ALOS/PALSAR interferograms from two ascending image pairs and one descending pair. All figures in this paper were generated with GMT[27] open-source software. **a**, Tectonic plates (after ref. 28) are Nazca (NZ), South American (SA), Scotia (SC) and Antarctic (AN). NZ converges on SA at a rate of about 68 mm yr^{-1} (ref. 29) as shown by the white arrow. The approximate rupture area of the M_w 9.5 1960 earthquake[30] is labelled EQ. The detailed study area in Fig. 2 is indicated by the red box. **b**, Interferogram from ascending path 121 orbits 09599 (2007 November 13) and 21677 (2010 February 18) with a perpendicular baseline ($B_\perp$) of 130 m. The direction of the satellite trajectory is shown by the red arrow labelled 'Az' in each panel. The line-of-sight look direction from the satellite to the ground is shown with the red arrow labelled 'LOS'. The black line labelled LOFZ marks the main strand of the LOFZ. Dashed black lines mark Michimahuida caldera (after ref. 6) and the smaller Chaitén caldera. **c**, Interferogram from ascending path 121 orbits 10941 (2008 February 13) and 23019 (2010 May 21) with a $B_\perp$ of 404 m. **d**, Interferogram from two descending path 417 orbits 09868 (2007 December 1) and 21946 (2010 March 8) with a $B_\perp$ of 41 m. The CMTs in Table 1 are plotted with the estimated two standard deviation error bars (http://www.globalcmt.org). **e**, Schematic explanation of the variable visibility of the deformation field between ascending and descending interferograms. Earth's surface is the dashed black line, a ray from the descending radar beam is labelled 'Desc-LOS' and a ray from the ascending radar beam is labelled 'Asc-LOS'. The collapsing sill-like body is red and the resulting deformation is depicted with red arrows.

the ascending-mode interferograms. The radar beams from both modes intersect the Earth's

surface at an angle of about 39° from the vertical. In the descending mode the satellite looks to the WNW, whereas in the ascending mode it looks to the ENE (red arrows in Fig. 1b–d).

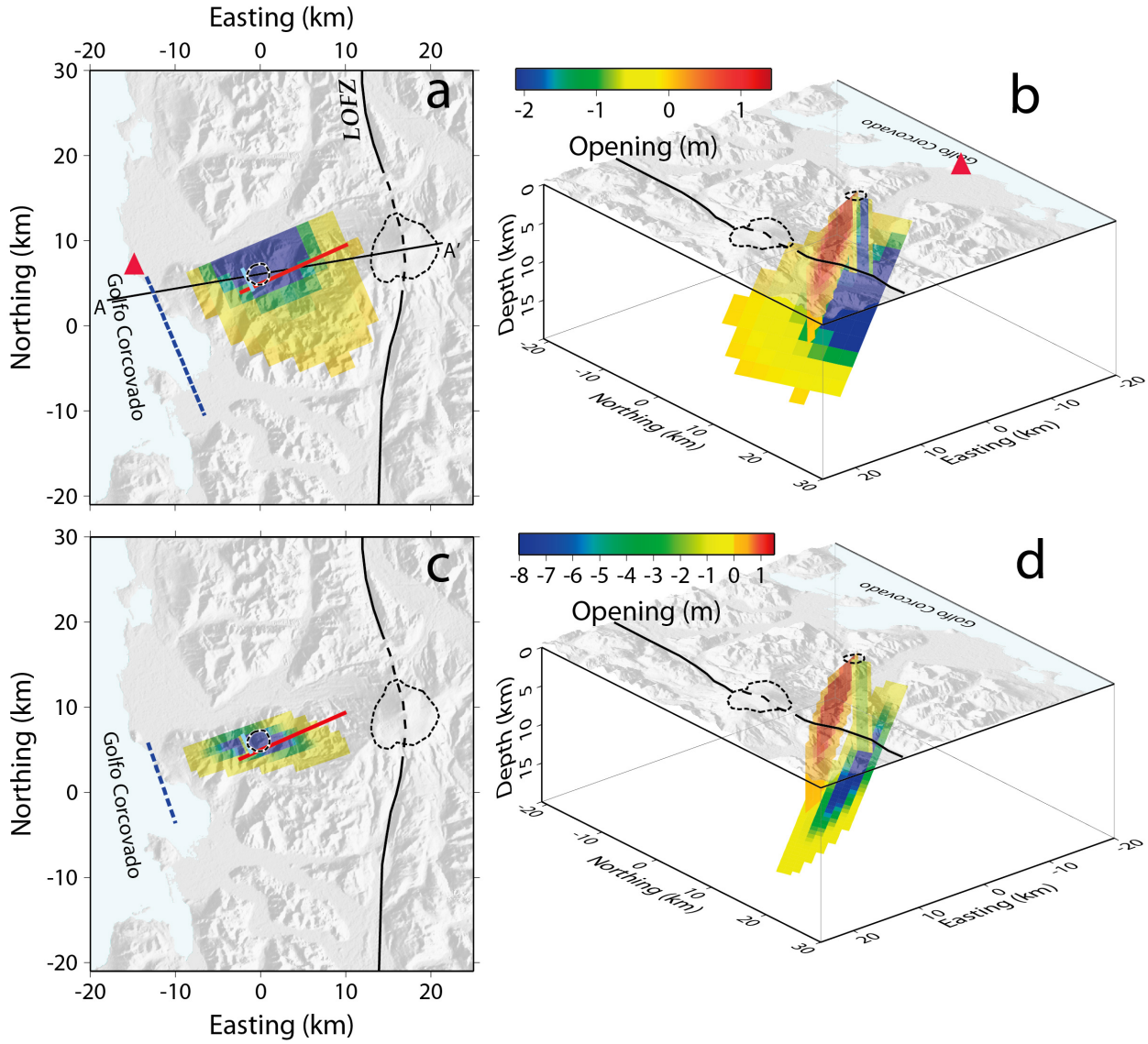

Figure 2 | Two deformation models that can be considered as near endmembers in a family of 'best-fit' models. Each model is composed of three planar bodies of distributed plane perpendicular opening or closing: a deep, dipping reservoir, a dyke and a narrow lath-like conduit (as discussed in the text). The outline of Michimahuida and Chaitén calderas and the approximate location of the LOFZ are shown (as discussed in Fig. 1). **a**, Plan view of the best-fit model in which the peak collapse in the deep body is constrained to 2 m. The surface trace of the dyke is red and the surface trace of the lath-shaped body is cyan. The plane containing the deep, dipping reservoir is projected to reach the surface at the dashed blue line. It dips about 40° to the ENE and is about 10 km deep below Chaitén. The red triangle near the dashed blue line shows the location of Morro Vilcún. The black line through the two calderas shows the location of cross-section A–A′ in Fig. 3. **b**, Perspective view of the model shown in **a** viewed from the NE. **c**, Plan view of the best-fit model in which the peak collapse in the deep body is constrained to 8 m (see also Supplementary Fig. 4). The red, cyan and dashed blue lines are as described in **a**. The reservoir dips about 45° to the ENE and is about 12 km deep below Chaitén. **d**, Perspective view of the model shown in **c**.

Consideration of the radar geometry, shown schematically in Fig. 1e, yields two important points: first, the deformation source responsible for the broad deformation signal is not an equidimensional volumetric source, and second, it should be a sill-like collapsing source that

dips to the ENE with a dip angle that is nearly complementary to the radar incidence angle in the ascending geometry.

Assuming an Earth model that is a uniform homogeneous elastic half-space, we determined that three separate deforming bodies were required to fit the data: first, a collapsing sill-like body (the 'reservoir') dipping to the ENE (that is, seeming to feed magma diagonally upwards from about 20 km depth beneath Michimahuida); second, a near-vertical expanding dyke trending to the ENE and extending from the deeper reservoir to the surface at Chaitén volcano; and third, a collapsing steeply dipping lath-shaped body (the 'conduit') surfacing near the west rim of the Chaitén caldera (Fig. 2). The dip of the reservoir is between 31° and 57° (Supplementary Fig. 3) to the ENE and the depth of the reservoir directly below Chaitén volcano is between 8 and 12 km. Apparent overshoot of the reservoir up-dip from the conduit is supported by modelling (see Methods) and by the presence of a string of NNW-trending undated rhyolitic plugs (the most prominent being Morro Vilcún) located where the reservoir fault should reach the surface (Figs 2a, b and 3a). This indicates that rhyolite might have migrated the length of the reservoir fault during a past eruption episode. The maximum amount of collapse on the reservoir is not well determined but can be roughly bounded. In Fig. 2 we show two equally viable models with a variable distribution of collapse on the reservoir. The model shown in Fig. 2a, b is the result of constraining the maximum collapse to be 2 m, whereas the model shown in Fig. 2c, d and Supplementary Fig. 4 is the result of constraining the maximum collapse to be 8 m. The fit to the data is essentially identical for each model and for all intervening values of maximum collapse, with a variance for the residual of about 3 cm^2 for each model and with each

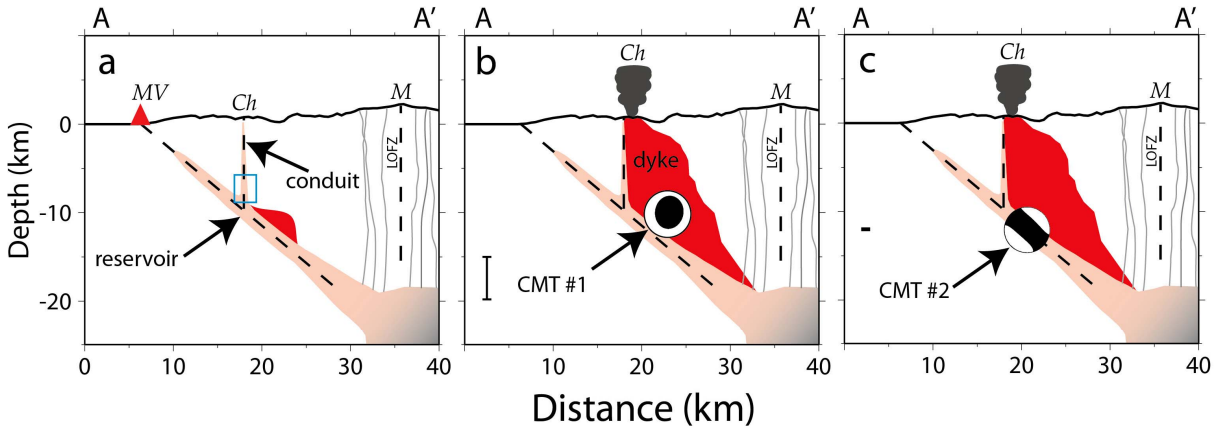

Figure 3 | Schematic interpretation of the involvement of deformation sources in the 2 May 2008 eruption of Chaitén. The location of cross-section A–A′ is shown in Fig. 2a; the positions of Morro Vilcún (MV), Chaitén (Ch) and Michimahuida (M) are labelled on the elevation profile. The dashed black lines show the approximate location of the LOFZ and inferred fault splays. The salmon-coloured area is the rhyolite reservoir that grades into a zoned magma chamber beneath Michimahuida. **a**, The blue box beneath Chaitén shows the approximate location of the cluster of seismicity located previously[14]. The dipping rhyolite reservoir and the lath-like conduit are discussed in the text. The seismicity, beginning on 30 April 2008 (ref. 2) indicates the initiation of dyking (coloured red) into rock above an inflated dipping sill. **b**, Continued dyking leads to the injection earthquake (projection of CMT 1 (Table 1) in the azimuth of the dyke is shown) just over 2 h before the explosive eruption. The dyke, roughly in the plane of the page, impinges on a vertical strand of the LOFZ beneath Chaitén, the location of the narrow lath-like conduit. **c**, On 3 May, nearly 19 h after the main Plinian eruption began, the dipping sill collapses catastrophically (projection of CMT 2 (Table 1) in the direction of the down-dip azimuth for the deep collapse body is shown) after a critical amount of magma has been withdrawn. The two standard deviation error bars for the CMT depths are shown at the left of **b** and **c**.

model accounting for about 98% of the data variance (Supplementary Figs 1, 2 and 5). The two

models in Fig. 2 represent loose bounds on a family of best-fit models with a maximum collapse between 2 and 8 m on the deep collapse body; the variance of the misfit increases for a maximum collapse of less than about 2 m or greater than about 8 m. As of about March 2010, the net decrease in volume represented by the three sources in the model is (150–250) $\times 10^6$ m^3. The estimated volume of material erupted during the May 2008 Plinian eruption[7,8] plus the new dome[2] is about (700–900) $\times 10^6$ m^3. It is tempting to attribute this difference to magma recharge; however, this observed relationship between change in reservoir volume and erupted volume is an expected consequence of magma compressibility[9].

Because of a lack of nearby seismic instrumentation, earthquake locations during the beginning phases of the eruption are not useful for additional constraints on the deformation sources. However, centroid moment tensor (CMT) solutions, recorded for the largest earthquakes, are consistent with our model. Only two earthquakes in the study area were large enough for CMT solutions to be calculated at the Global CMT Project (http://www.globalcmt.org) (Table 1 and Fig. 1d). CMT 1 (Fig. 1d and Table 1) is the solution for an earthquake of moment magnitude (M_w) 5.2 that occurred about 2 h before the main explosive event at 08:00 UT on 2 May 2008 (ref. 2). CMT 2 (Fig. 1d and Table 1) is the solution for a M_w 5.0 earthquake that occurred about 19 h after the onset of the main explosive event. Because each CMT solution includes a large compensated linear vector dipole component (CLVD), and because of the timing of the earthquakes in an eruption setting, we interpret the CMT solutions to be a magma injection (dyking) event (CMT 1) and a reservoir collapse event (CMT 2). The CLVD contribution to the total moment of an earthquake is measured by the value ε in Table 1, where $\varepsilon = |2\lambda_3/\lambda_1|$ and the eigenvalues of the moment tensor are λ_1, λ_2 and λ_3 ($|\lambda_1| \geq |\lambda_2| \geq |\lambda_3|$). An ε value of 1.0 is a CMT with only a CLVD, and a value of 0 is a conventional shear-failure double-couple mechanism (see, for example, ref. 10). It has been shown[10] that a m_b = 5.5 magma-injection earthquake, under the assumption of no net change in volume (or a trace of zero, as is assumed for Global CMT Project CMT solutions), could be best represented by a CLVD. CMT 1 is consistent with a near vertical dyke that trends to the ENE, the same as our modelled dyke (Fig. 3). CMT 2 is consistent with a collapsing sill-like body that dips roughly 42° to the ENE, the same as our modelled deep sill-like reservoir (Fig. 3 and Supplementary Fig. 3). As noted previously[11], seismic data can be used to determine an accurate earthquake mechanism, but accurate earthquake locations cannot be determined without instrumentation close to the source. The location and depth of CMT solutions have been shown to be biased by tens of kilometres in remote locations[12,13]. In Fig. 3 we plot the CMT mechanisms projected in the cross-section geometry with the realization that depths are probably biased.

Further support for the presence of the lath-like conduit was presented previously[14]: a network of seismometers was deployed in the area of Chaitén volcano for 11 months from December 2004 to November 2005. This temporary network enabled the location of a cluster of seismicity directly beneath Chaitén volcano that spanned a depth interval from the top of our

inferred dipping reservoir to about 5.5 km depth (Fig. 3a). This seismicity coincides with the location of the narrow conduit in our model and might indicate ongoing inflation during the buildup to the eruption. One of the earthquakes roughly 8.5 km beneath Chaitén was large enough (M_w 3.56) for a moment tensor solution to be determined[14]. The CLVD component could not be resolved, but the geometry was roughly consistent with strike-slip movement on either the fault surface containing the narrow lath-like conduit or a possible fault surface containing the dyke.

The nature of the inferred faults in Figs 2 and 3, west of the LOFZ, might be similar to those defined in recent studies[4,5] that outlined pop-up structures at latitudes immediately south of the Michimahuida–Chaitén volcanic complex. The pop-up structures are defined by a structural high centred on the LOFZ that is bounded on the west by east-dipping reverse faults and on the east by west-dipping reverse faults that merge at depth with the LOFZ. Vertical shear structures are found between the reverse faults. Alternatively, the inferred faults could be part of a fault complex that occurs between two separate north–south branches of the LOFZ[15]: one branch is as shown in the figures and the other branch could extend northwards into the study area beneath the Golfo Corcovado. We interpret the dipping sill-like reservoir as containing rhyolitic magma that occupies an ENE-dipping reverse fault that is related to the LOFZ. If this is so, the rhyolite reservoir would tap a zoned magma body[16] under Michimahuida that is the site of basalt/andesite influx. The reverse fault is an effective path for magma migration and the segregation of low-density melt. Fault involvement and tectonic control in the Chaitén eruption have been proposed previously[17].

Petrological experiments[1] on the pumice ejected during the initial Chaitén Plinian eruption indicate that the material came from a depth of about 5–9 km in less than about 4 h. This depth range is consistent with a magma source from the deep, dipping, sill-like reservoir beneath Chaitén. The earthquake for which a dyking CMT mechanism was recorded (CMT 1: Figs 1d and 3b and Table 1), just over 2 h before the main Plinian eruption, indicates that the rapid transport of magma was accomplished through dyking. After the dyking event, rhyolite magma was rapidly evacuated from the reservoir until it partly collapsed, causing the earthquake represented by CMT 2 (Figs 1d and 3c and Table 1). The first erupted material was an ash fall noted about 11 h before the main Plinian eruption[1]; this pre-Plinian ash flow might have come from the lath-like conduit, before the dyke reached the surface (between the situations shown in Fig. 3a, b).

Table 1 | Centroid moment tensor solutions from Global CMT Project

CMT (Figs 1d and 3)	Origin time (UT)	Latitude	Longitude	Depth (km)	M_w	Eigenvalues λ_1, λ_2, λ_3	ε
1	2008/05/02 05:51	42.93° S	72.65° W	17.4	5.2	1.10, –0.74, –0.36	0.65
2	2008/05/03 02:36	42.82° S	72.56° W	12.0	5.0	–5.68, 3.58, 2.10	0.74

Our model of the magmatic system beneath Chaitén favours a common crustal magma chamber for Chaitén and Michimahuida, both of which erupt on a timescale of hundreds to thousands of years. Basalt intrusions into the magma chamber beneath Michimahuida must occur

frequently to keep Michimahuida active, but how these intrusions promote rhyolite exfiltration towards the Chaitén reservoir remains obscure. We speculate that crustal tectonics could have a two-way role in reshearing the LOFZ pop-up structure, assisted by magmatic overpressure, and draining the rhyolite from a more mafic mush. Alternatively, some event such as the 1960 earthquake could lead to the formation of the Chaitén magma reservoir by the mechanical introduction of permeability and a pressure gradient around an overpressured magma body beneath Michimahuida. Large subduction earthquakes occur on a scale of hundreds of years in this part of Chile[18]. In the latter situation, the rhyolitic magma body beneath Chaitén has been filling since the great 1960 Chilean earthquake (Fig. 1) until the resulting overpressure exceeded the overlying rock strength in May 2008.

METHODS SUMMARY

To model the interferograms, we first resampled the InSAR data by using a quadtree algorithm, thus reducing the large number of highly correlated data points in each InSAR image[19,20] (Supplementary Figs 1 and 2). We conducted preliminary exploratory modelling using one, two and three rectangular sources of uniform opening and closing[21]. The addition of the third source markedly reduced the variance of the residual compared with one and two sources. We then further investigated a model consisting of three independent patches of distributed opening or closing. Each distribution is described functionally by a two-dimensional Weibull distribution that includes a covariance (or interaction) parameter[22,23]. We used a constrained Monte Carlo nonlinear inversion scheme to find the location, strike, dip, maximum opening or closing and Weibull parameters for each distribution of opening or closing, a truncation parameter for each distribution (allowing some or all of the distribution to be of uniform opening or closing), and static shift and tilt parameters for each interferogram. This method allowed us to search a wide range of model geometries and distributions automatically and it also enabled the automatic modelling of sharp spatial discontinuities in opening or closing. In the limiting cases the two-dimensional Weibull distribution[22] can be a point source, a line source or an area of uniform opening or closing, but it can also be a teardrop-shaped[24] or tadpole-shaped[25] dyke (Supplementary Fig. 4). The significance of misfit and uncertainties in model parameters discussed in the text were found by means of an *F*-test and a 95% probability. It has been shown[26] that the quadtree parsed data can be treated as independent data points, allowing us to use this method of uncertainty estimation (however, see Methods and Supplementary Fig. 3).

Received 12 March; accepted 30 August 2011; doi:10.1038/nature10541

1. Castro, J. M. & Dingwell, D. B. Rapid ascent of rhyolitic magma at Chaitén volcano, Chile. *Nature* **461,** 780–784 (2009).
2. Carn, S. A. *et al.* The unexpected awakening of Chaitén volcano, Chile. *Eos* **90,** 205–212 (2009).
3. Cembrano, J., Hervé, F. & Lavenu, A. The Liquiñe–Ofqui fault zone: a long lived intraarc fault system in southern Chile. *Tectonophysics* **259,** 55–66 (1996).

4. Cembrano, J. *et al.* Late Cenozoic transpressional ductile deformation north of the Nazca–South America–Antarctica triple junction. *Tectonophysics* **354,** 289–314 (2002).
5. Thomson, S. N. Late Cenozoic geomorphic and tectonic evolution of the Patagonian Andes between latitudes 42°S and 46°S: an appraisal based on fission-track results from the transpressional intra-arc Liquiñe–Ofqui fault zone. *Geol. Soc. Am. Bull.* **114,** 1159–1173 (2002).
6. Kilian, R. & Lopez-Escobar, L. Petrology of the Southern SouthAndean Volcanic Zone (41–46° S) with emphasis on the Michinmáhuida–Chaitén complex (43° S). *Zbl. Geol. Paläont. I* **1991,** 1693–1708 (1992).
7. Watt, S. F. L., Pyle, D. M., Mather, T. A., Martin, R. S. & Matthews, N. E. Fallout and distribution of volcanic ash over Argentina following the May 2008 explosive eruption of Chaitén, Chile. *J. Geophys. Res.* **114,** B04207, doi:10.1029/2008JB006219 (2009).
8. Alfano, F. *et al.* Tephra stratigraphy and eruptive volume of the May, 2008, Chaitén eruption, Chile. *Bull. Volcanol.* **73,** 613–630 (2011).
9. Mastin, L. G., Roeloffs, E., Beeler, N. M. & Quick, J. E. in *A Volcano Rekindled: The Renewed Eruption of Mount St. Helens, 2004–2006* (eds Sherrod, D. R., Scott, W. E. & Stauffer, P. H.) 461–488 (US Geol. Surv. Prof. Pap. 1750, 2008).
10. Kanamori, H., Ekstrom, G., Dziewonski, A., Barker, J. S. & Sipkin, S. A. Seismic radiation by magma injection: an anomalous seismic event near Tori Shima, Japan. *J. Geophys. Res.* **98,** 6511–6522 (1993).
11. Lohman, R. B., Simons, M. & Savage, B. Location and mechanism of the Little Skull Mountain earthquake as constrained by satellite radar interferometry and seismic waveform modeling. *J. Geophys. Res.* **107,** 2118, doi:10.1029/2001JB000627 (2002).
12. Lohman, R. B. & Simons, M. Locations of selected small earthquakes in the Zagros mountains. *Geochem. Geophys. Geosyst.* **6,** Q03001, doi:10.1029/2004GC000849 (2005).
13. Legrand, D., Barrientos, S., Bataille, K., Cembrano, J. & Pavez, A. The fluid-driven tectonic swarm of Aysen Fjord, Chile (2007) associated with two earthquakes (Mw=6.1 and Mw=6.2) within the Liquiñe-Ofqui Fault Zone. *Cont. Shelf Res.* **31,** 154–161 (2011).
14. Lange, D. *et al.* First seismic record for intra-arc strike-slip tectonics along the Liquiñe-Ofqui fault zone at the obliquely convergent plate margin of the southern Andes. *Tectonophysics* **455,** 14–24 (2008).
15. Cembrano, J. & Lara, L. The link between volcanism and tectonics in the southern volcanic zone of the Chilean Andes: a review. *Tectonophysics* **471,** 96–113 (2009).
16. Hildreth, W. Gradients in silicic magma chambers: implications for lithospheric magmatism. *J. Geophys. Res.* **86,** 10153–10192 (1981).
17. Lara, L., Pallister, J. S. & Ewert, J. W. The 2008 eruption of Chaitén volcano, Southern Chile: a tectonically controlled eruption. *Eos* **89,** *Fall Meet. Suppl.*, abst. V42C-02**,** (2008).
18. Cisternas, M. *et al.* Predecessors of the giant 1960 Chile earthquake. *Nature* **437,** 404–407 (2005).

19. Jónsson, S., Zebker, H., Segall, P. & Amelung, F. Fault slip distribution of the 1999 Mw 7.1 Hector Mine, California, earthquake, estimated from satellite radar and GPS measurements. *Bull. Seismol. Soc. Am.* **92,** 1377–1389 (2002).
20. Simons, M., Fialko, Y. & Rivera, L. Coseismic deformation from the 1999 Mw7.1 Hector Mine, California, earthquake as inferred from InSAR and GPS observations. *Bull. Seismol. Soc. Am.* **92,** 1390–1402 (2002).
21. Okada, Y. Surface deformation due to shear and tensile faults in a half-space. *Bull. Seismol. Soc. Am.* **75,** 1135–1154 (1985).
22. Myrhaug, D. & Rue, H. Joint distribution of successive wave periods revisited. *J. Ship Res.* **42,** 199–206 (1998).
23. Brodtkorb, P. A. *et al.* in *Proceedings of the 10th International Offshore and Polar Engineering conference, Seattle* (eds Chung, J. S., Frederking, R. M. W., Saeki, H. & Koterayama, W.) Vol. 3, 343–350 (International Society of Offshore and Polar Engineers, Cupertino, CA USA, 2000).
24. Weertman, J. Theory of water-filled crevasses in glaciers applied to vertical magma transport beneath oceanic ridges. *J. Geophys. Res.* **76,** 1171–1183 (1971).
25. Rubin, A. M. Propagation of magma-filled cracks. *Annu. Rev. Earth Planet. Sci.* **23,** 287–336 (1995).
26. Jónsson, S. *Modeling Volcano and Earthquake Deformation from Satellite Radar Interferometric Observations*. PhD thesis, Stanford Univ. (2002).
27. Wessel, P. & Smith, W. H. F. Free software helps map and display data. *Eos* **72,** 441 (1991).
28. Bird, P. An updated digital model of plate boundaries. *Geochem. Geophys. Geosyst.* **4,** 1027, doi:10.1029/2001GC000252 (2003).
29. Ruegg, J. C. *et al.* Interseismic strain accumulation measured by GPS in the seismic gap between Constitución and Concepción in Chile. *Phys. Earth Planet. Inter.* **175,** 78–85 (2009).
30. Barrientos, S. E. & Ward, S. N. The 1960 Chile earthquake: inversion for slip distribution from surface deformation. *Geophys. J. Int.* **103,** 589–598 (1990).

Supplementary Information is linked to the online version of the paper at www.nature.com/nature.

Acknowledgements We thank D. Dzurisin, Z. Lu and W. Thatcher for providing helpful comments on the manuscript. All ALOS/PALSAR data are copyright JAXA and the Japanese Ministry of Economy, Trade and Industry (2008, 2009, 2010) and were provided by the Alaska Satellite Facility. The data were made available through JAXA project PI059 and the U. S. Govt. Sponsored Research Consortium data pool supported by NASA, the National Science Foundation and the US Geological Survey.

Author Contributions C.W. coordinated the research and writing of the paper. All authors contributed to the interpretation of results and writing of the paper.

Author Information Reprints and permissions information is available at www.nature.com/reprints. The authors declare no competing financial interests. Readers are welcome to comment on the online version of this article at www.nature.com/nature. Correspondence and requests for materials should be addressed to C.W. (cwicks@usgs.gov).

METHODS

Modelling

To model the interferograms, we first resampled the InSAR data by using a quadtree algorithm, thus reducing the large number of highly correlated data points in each InSAR image[19,20] (Supplementary Figs 1 and 2). We conducted preliminary exploratory modelling using one, two and three rectangular sources of uniform opening and closing[21]. The addition of the third source markedly reduced the variance of the residual compared with one and two sources. We then further investigated a model consisting of three independent patches of distributed opening or closing. Each distribution is described functionally by a two-dimensional Weibull distribution that includes a covariance (or interaction) parameter[22,23]. We used a constrained Monte Carlo nonlinear inversion scheme to find the location, strike, dip, maximum opening or closing and Weibull parameters for each distribution of opening or closing, a truncation parameter for each distribution (allowing some or all of the distribution to be of uniform opening or closing), and static shift and tilt parameters for each interferogram. This method allowed us to search a wide range of model geometries and distributions automatically and it also enabled the automatic modelling of sharp spatial discontinuities in opening or closing. In the limiting cases the two-dimensional Weibull distribution[22] can be a point source, a line source or an area of uniform opening or closing, but it can also be a teardrop-shaped[24] or tadpole-shaped[25] dyke (Supplementary Fig. 4).

Because the CMT solutions support the presence of the dipping reservoir and the dyke, but not the conduit, we tried modelling the InSAR data with only two sources. Models consisting of only two deforming bodies yielded a significantly worse fit, assuming the quadtree data are independent[26], with less than a 1 in 10^9 chance that the higher variance compared with the best-fit models could be attributed to random fluctuations in the data. The collapsing conduit is a necessary feature. Before descending data were available over Chaitén, it was found[31] that the model that best fitted the ascending ALOS data (Fig. 1b, c), out of several models ranging from a point pressure source to models including slip, was a narrow steeply dipping uniform collapsing rectangular dyke, similar to the conduit in our model. We also modelled the data with a dyke and a listric fault (a curved surface) occupied by both the conduit and the reservoir, but the fit to the data was significantly worse than the best-fit models, with about a 1 in 10^6 chance that the higher variance compared with the best-fit models could be attributed to random fluctuations in the data. The conduit and reservoir are therefore not continuous on a curved surface, and the overshoot of the large ENE dipping reservoir up-dip from the conduit is a required feature.

Uncertainties

The significance of misfit and uncertainties in model parameters discussed in the text were found by means of an *F*-test and a 95% probability. It has been shown[26] that the quadtree parsed data can be treated as independent data points, allowing us to use this method of uncertainty

estimation (Supplementary Fig. 3); however, correlated noise might bias these estimates. To address concerns that correlated noise in the interferograms might affect our uncertainty estimates, we use a method of model parameter uncertainty estimation that involves estimating noise covariance for each interferogram (for background on the method see refs 26, 32, 33). We first found a covariance function for each interferogram using data outside the deforming area, then approximated the covariance function $C(r)$ with an simple exponential decay function[33] $C(r) = \sigma^2 e^{-\alpha r}$, where r is the distance between data points, σ^2 is the variance and α is the decay constant. We then constructed noise covariance matrices for each interferogram, from which we propagated noise covariance matrices for the quadtree data for each interferogram (Supplementary Figs 6a and 7a). Using the quadtree covariance matrices (following refs 32, 33) we calculated possible realizations of correlated noise for each quadtree point (Supplementary Figs 6b and 7b), added the noise to the data, and then found the resulting optimal model. We performed this procedure 100 times and plotted the distribution of dips for the dipping reservoir, which has been taken to represent the error (Supplementary Fig. 3). If the noise covariance estimates of uncertainty are accurate and if the *F*-test uncertainties are biased by uncorrelated noise, we would expect the *F*-test uncertainty intervals to be narrower than the noise covariance uncertainty intervals. However, comparison of the dip uncertainty intervals reveals that the range of uncertainties in dip using the noise covariance is much narrower than the range of *F*-test uncertainties. We suggest that the noise covariance method of uncertainty estimation either does not properly interrogate the data structure or does not thoroughly investigate the trade-off in model parameters (or both). Further investigation of these differences requires more study beyond the scope of this paper. In the worst case, the noise covariance uncertainties represent an additional ±4° of uncertainty to our *F*-test uncertainties of about ±13°; this would put the uncertainties close to the red line in Supplementary Fig. 3. From this comparison of uncertainties, we conclude that the role of uncorrelated noise on our *F*-test uncertainties is small (at the worst) and does not change our interpretation or conclusions.

31. Fournier, T. J., Pritchard, M. E. & Riddick, S. N. Duration, magnitude, and frequency of subaerial volcano deformation events: new results from Latin America using InSAR and a global synthesis. *Geochem. Geophys. Geosyst.* **11,** Q01003, doi:10.1029/2009GC002558 (2010).
32. Lohman, R. B. & Simons, M. Some thoughts on the use of InSAR data to constrain models of surface deformation: noise structure and data downsampling. *Geochem. Geophys. Geosyst.* **6,** Q01007, doi:10.1029/2004GC000841 (2005).
33. Parsons, B. *et al.* The 1994 Sefidabeh (eastern Iran) earthquakes revisited: new evidence from satellite radar interferometry and carbonate dating about the growth of an active fold above a blind thrust fault. *Geophys. J. Int.* **164,** 202–217 (2006).